# Highly selective separation of benzene/cyclohexane by 3D covalent organic framework with 8,8-connected bcu net topology

Yu Zhao,[a,b,+] Tsukasa Irie,[c,+] Dan Wen,[a,b,+] Haruna Mabuchi,[c] Koki Sasaki,[c] Mika Nozaki,[c] Rina Tomioka,[c] Weidong Zhu,[a,b] Saikat Das,*[d] Teng Ben*[a,b] and Yuichi Negishi*[c,d]

[a]Zhejiang Engineering Laboratory for Green Syntheses and Applications of Fluorine-Containing Specialty Chemicals, Institute of Advanced Fluorine-Containing Materials, Zhejiang Normal University, 321004 Jinhua, China

[b]Key Laboratory of the Ministry of Education for Advanced Catalysis Materials, Institute of Physical Chemistry Zhejiang Normal University Jinhua 321004, China

[c]Department of Applied Chemistry, Faculty of Science, Tokyo University of Science, Kagurazaka, Shinjuku-ku, Tokyo 162-8601, Japan

[d]Research Institute for Science & Technology, Tokyo University of Science, Kagurazaka, Shinjuku-ku, Tokyo 162-8601, Japan

[+]These authors contributed equally.

***Corresponding author**

Email: saikatdas@rs.tus.ac.jp; tengben@zjnu.edu.cn; negishi@rs.tus.ac.jp

**ABSTRACT:** Covalent assembly of organic linkers with higher denticity toward three-dimensional (3D) covalent organic framework (COF) nets of increasing connectivity can not only elevate the architectural intricacy of the framework but also impart it with unprecedented functionalities. The synthesis of highly-connected 3D COFs is in its incipient stage and the 3D COFs built from octadentate linkers are limited to (8,2), (8,3) and (8,4)-connected nets. Here we report the discovery of the first (8,8)-connected 3D COF, TUS-88, having **bcu** topology by linking an 8-connected $D_{4h}$-symmetric quadrangular prism node to an 8-connected $D_{2h}$-symmetric tetragonal prism node. Derived from the π-aromatic conjugated system of pyrene and the abundant aromatic phenyl rings composing the COF scaffold which promotes to stronger π···π interactions with aromatic benzene (Bz) molecules, a superlative Bz uptake of 1618 mg $g^{-1}$ was achieved for TUS-88, coupled with exemplary cyclohexane (Cy) uptake of 842 mg $g^{-1}$ and ideal Bz/Cy selectivity of 1.92 which are the current benchmark. Breakthrough experiments accomplished using Bz/Cy (1:1, v/v) mixture corroborated the preferential adsorption of Bz by the COF from the mixture to generate high purity Cy with a significant time interval of 75.4 min $g^{-1}$ and record-setting Bz/Cy breakthrough selectivity of 2.46.

## 1. Introduction

Hailed as one of the seven chemical separations that can change the world,[1] the selective separation of hydrocarbons with almost identical physical properties, as exemplified by benzene (Bz) and cyclohexane (Cy), is intensely demanding. Bz has gained widespread recognition as a leading industrial chemical for its prime role as intermediate in the preparation of a myriad of chemicals like ethylbenzene, aniline, nitrobenzene, cyclohexane, styrene, cumene etc. and the greater usage of benzene derivatives in the automotive sector for the production of synthetic rubber, as reflected from its surging demand with an expected compound annual growth rate (CAGR) of 3.81% through 2030.[2] On the other hand, Cy is of high industrial interest as a feedstock for the production of ε-caprolactam and adipic acid, the raw materials used to make nylon 6 and nylon 66.[3] The two potential routes to Cy production are: catalytic hydrogenation of Bz and fractional distillation of petroleum, the former being more prevalent.[4] Incomplete hydrogenation of Bz owing to a shift of the thermodynamic equilibrium towards Bz at reaction temperature above 573 K accompanies to the existence of unreacted Bz in the product stream, which calls for removal of the unreacted Bz to get high-purity Cy.[5] Nonetheless, the strikingly similar boiling points (Bz: 353.25 K, Cy: 353.85 K),[6] molecular dimensions (Bz: 3.3 × 6.6 × 7.3 $Å^3$, Cy: 5.0 × 6.6 × 7.2 $Å^3$)[7] and collision diameters (Bz: 5.26 Å, Cy: 6.06 Å)[8] of the two pose insurmountable challenges to their separation. The high propensity of Bz to form azeotrope with Cy (at 45% Cy) characterized by a constant boiling point of 350.65 K is an added hassle.[9] That being the case, ordinary distillation technique lacks the capacity to separate Bz and Cy. Extractive distillation and azeotropic distillation are currently deployed for Bz/Cy separation; however, they still have many shortcomings. Notwithstanding that extractive distillation can competently separate Bz and Cy inasmuch as the entrainers can change the relative volatilities of the components, the common entrainers such as organic solvents are beset with high toxicity and volatility while the high production costs of ionic liquids is a major concern.[10] On the other hand, azeotropic distillation operates effectively only when the Bz concentration is over 90%, in addition to the concerns over complex systems and severe energy burden.[10] Liquid-liquid extraction is appealing for Bz/Cy separation owing to its energy-efficiency and its applicability in particular when the Bz concentration is below 20 wt%[4,11]; however, it might not be worthwhile for industrial practices.[10] Imparting with high separation factors and not limited to vapor-liquid equilibrium, membrane-based separation methods like pervaporation and perstraction are worthwhile alternatives to distillation for Bz/Cy separation, with the former being more beneficial owing to lower membrane area requirements.[8,12,13] However, it is still imperative to integrate membrane methods with distillation in order to separate a binary Bz/Cy mixture into its two constituents with high purity.[13] On the basis thereof, the present challenge in Bz/Cy separation is to seek an alternative method with high selectivity, simple operation and energy-efficiency.

Crafted from organic building units that are stitched together by robust bonds to develop open scaffolds encompassing porosity, covalent organic frameworks (COFs) epitomize crystalline porous polymers with a diverse structure and application portfolio.[14-27] The large internal surface areas, precisely designable pore profile, and tailorable functionalities of COFs can be leveraged for selective separation of guest molecules.[28-31] The ease of synthesis and crystal structure determination of two-dimensional (2D) COFs had oriented the decade-and-a-half of COF research chiefly towards 2D COFs, failing to adequately provide for three-dimensional (3D) architectures. Nevertheless, the performance of 2D COFs is often hampered by layer offset or stacking faults, which impedes the diffusion paths, and restricts the accessibility of functional sites and interactions between pore walls and guest molecules.[32] Contrarily, 3D COFs featuring superior specific surface areas, interconnecting pore nanochannels enabling molecular transport along three directions, diverse channel architecture and facilely accessible active sites might be more rewarding for separation applications.[33] Simultaneously, the top-notch stability stemming from the covalent connectivity of COF scaffolds give them an edge over metal-organic framework (MOF) physisorbents to study Bz/Cy selectivity. That said, the repertoire of 3D COFs is rather limited because unlike MOFs that harness

metal-organic polyhedra as supermolecular building blocks with connectivity as high as 24,[34] the points of extension of 3D COF linkers is yet no greater than 8. The construction of highly connected 3D COF nets is in the early stages and the 3D COFs documented heretofore utilizing octatopic linkers are based on (8,2),[35,36] (8,3)[37] and (8,4)[38-40]-connected nets. Moreover, for the very few COFs that have yet been used in the adsorptive separation of Bz and Cy, the adsorption capacity is low, mostly limited to the Ideal Adsorbed Solution Theory (IAST) calculation, and the separation effect is rarely evaluated through experiments.[41-43] Under these circumstances, the discovery of new 3D COFs with rich aromatic conjugated structures, bespoke functionalities and suitable pore sizes is highly coveted for Bz/Cy separations.

In this study, we extend the connectivity of 3D COFs from the existing (8,2), (8,3) and (8,4) to (8,8). The assembly of 8-connected $D_{4h}$-symmetric quadrangular prism vertices and 8-connected $D_{2h}$-symmetric tetragonal prism vertices led to an exquisitely architected 3D COF, TUS-88 (TUS = Tokyo University of Science), having the 2-fold interpenetrated **bcu** topology (Figure 1). The **bcu-c** framework of TUS-88 exemplifies a regular periodic crystal lattice characterized by openly accessible pore cavities for trapping guest species and appreciable stability. The aromatic properties of pyrene and the phenyl rings making up the COF backbone which facilitates stronger π···π interactions with aromatic Bz molecules endow the COF with a top-notch Bz adsorption capacity, besides incredible Cy adsorption and ideal Bz/Cy selectivity. Breakthrough analysis for 1:1 Bz/Cy mixture evidenced the efficient separation of Bz over Cy affording pure Cy with a long retention time (75.4 min $g^{-1}$) of Bz and record-high Bz/Cy experimental selectivity of 2.46. Density functional theory (DFT) calculations bolstered our understanding of host-guest interaction dynamics with further evidence of binding energies corresponding to different types of interactions at different binding sites of the framework for both Bz and Cy molecules. This work can serve as a reference to reach even higher connected and more complex COF nets.

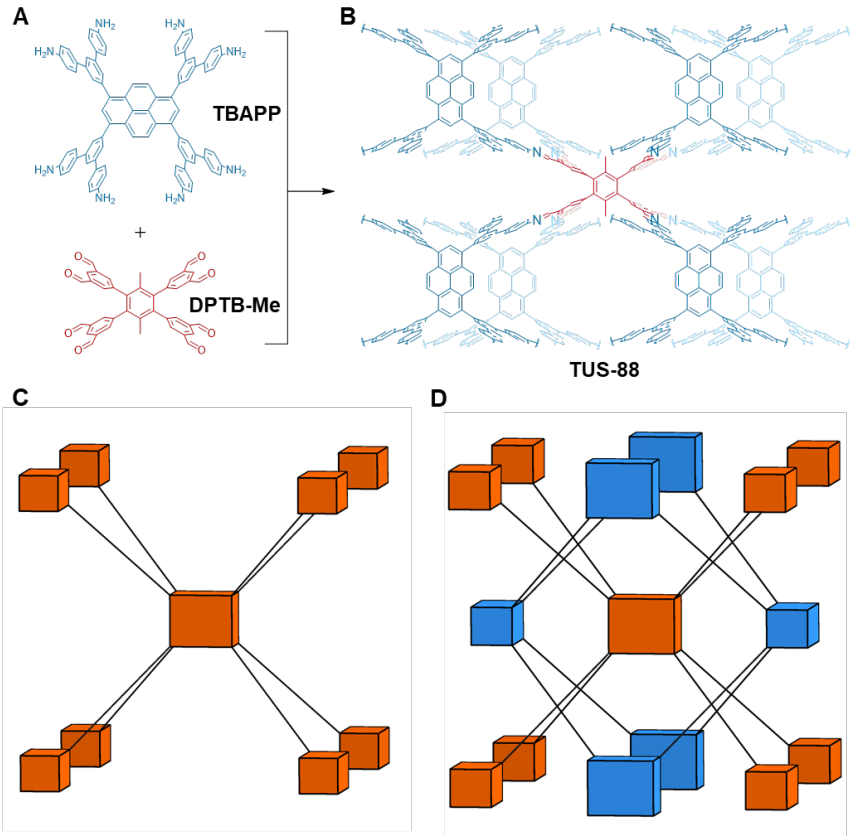

**Figure 1. The first (8,8)-connected 3D COF.** (A) Reticulation of an 8-connected $D_{4h}$-symmetric linker, TBAPP, with an 8-connected $D_{2h}$-symmetric linker, DPTB-Me, leading to (B) a (8,8)-connected 3D COF, TUS-88. (C) Non-interpenetrated and (D) 2-fold interpenetrated **bcu** nets.

## 2. Results and Discussion

### 2.1. Synthesis and Characterization of TUS-88

Determined through reaction optimization, the synthetic route for TUS-88 involved Schiff base condensation under solvothermal conditions of equimolar amounts of 1,3,6,8-tetrakis3,5-bis[(4-amino)phenyl]phenylpyrene (TBAPP) and 4',5′-bis(3,5-diformylphenyl)-3′,6′-dimethyl-[1,1′:2′,1″-terphenyl]-3,3″,5,5″-tetracarbaldehyde (DPTB-Me) employing *o*-dichlorobenzene (*o*-DCB) in the presence of aniline and 9 M aqueous acetic acid at 393 K for 7 days, furnishing a yellow crystalline powder in 88% isolation yield (see Experimental Procedures for details). The chemical connectivity of the imine bonds in the prepared COF was substantiated with evidence by Fourier transform infrared (FT-IR) and solid-state $^{13}C$ cross-polarization magic angle spinning (CP-MAS) NMR spectroscopies. FT-IR spectral trace for TUS-88 divulged the occurrence of a strong vibration band at 1622 $cm^{-1}$ ascribable to the C=N bonds. Concurrently, the amplitude of N−H stretching band at 3346 $cm^{-1}$ of TBAPP and C=O stretching band at 1705 $cm^{-1}$ of DPTB-Me were significantly diminished, providing evidence for the polycondensation reaction between TBAPP and DPTB-Me monomers (Figure S1). In addition, a new resonance at 160.7 ppm could be distinctly noticed in the $^{13}C$ CP/MAS NMR spectrum that characteristically appeared from the imine (C=N) carbon (Figure S2). Elemental analysis further reaffirmed the successful formation of the COF (Anal. Calcd. for $C_{128}H_{76}N_8$: C: 89.07; H: 4.44; N: 6.49. Found: C: 85.02; H: 4.49; N: 6.09). TUS-88 featured rice grain-like homogeneous morphology, as reflected from the scanning electron microscopy (SEM) (Figure S3) and transmission electron microscopy (TEM) (Figure S4A) micrographs. Thermogravimetric analysis (TGA) plot of TUS-88 acquired under a $N_2$ gas stream implied that its thermal stability could reach up to ~695 K (Figure S6). Besides, TUS-88 was able to sustain its crystallinity after immersing in a wide assortment of organic solvents, boiling water, 6 M HCl and 6 M NaOH for 24 hours, as observable from the persistent peaks in the powder X-ray diffraction (PXRD) profiles of the treated COF samples (Figure S7).

### 2.2. Crystal Structure Analysis

We comprehended the crystallographic structure and unit cell of the COF harnessing a combination of PXRD observations with structural modeling and Pawley refinement (Figure 2). Predicated on the topological structures cataloged in Reticular Chemistry Structure Resource (RCSR)[44], we arrived at the **bcu** net as the most plausible topology following from the assembly of two octatopic linkers with $D_{4h}$ and $D_{2h}$ symmetry. The structural models of TUS-88 were optimized through the Forcite program within the *Materials Studio* 7.0 software[45]. As can be noticed from Figure S15, the simulated diffraction pattern obtained from the 2-fold interpenetrated **bcu** net is in consensus with the experimental PXRD data. The optimization of TUS-88 led to a space group of *Cmmm* (No. 56) with unit cell parameters: $a$ = 19.0953 Å, $b$ = 18.9915 Å, $c$ = 23.0395 Å, $\alpha = \beta = \gamma = 90^o$ (Table S3). The experimental PXRD trace obtained for TUS-88 contained well-defined Bragg peaks at 4.55º, 6.51º, 7.73º, 9.09º, 12.97º and 13.05º that can be indexed with (100), (110), (002), (200), (210) and (220) reflections, respectively (Figure 2). Pawley refinement of the experimentally recorded diffraction pattern afforded the refined unit cell parameters: $a$ = 19.5200 Å, $b$ = 18.8401 Å, $c$ = 23.8180 Å, $\alpha = \beta = \gamma = 90^o$ and substantially low $R$-factors, $R_p$ = 2.96%, $R_{wp}$ = 3.91%. We scrutinized alternative structure solutions by considering the crystal model based on a non-interpenetrated **bcu** topology in *Pmmm* space group (No. 47) (Figures S19-S21, Table S4) but the calculated and experimental diffraction patterns were incompatible with each other (Figure S18). High-resolution TEM (HRTEM) coupled with fast Fourier transform (FFT) was conducted

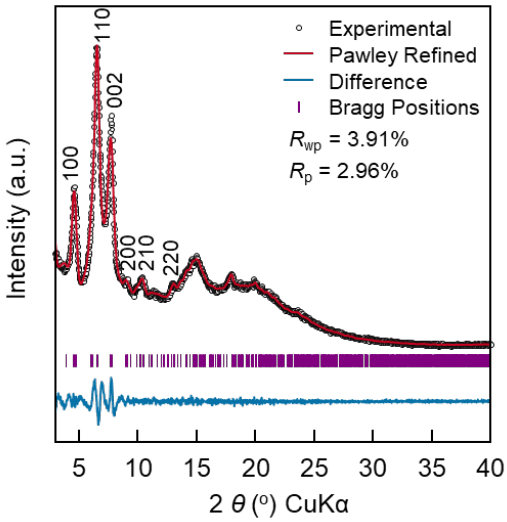


**Figure 2. PXRD patterns for TUS-88.** Experimental pattern (black circle), Pawley refined (red curve), difference plot (blue curve) between the experimental and refined patterns, and Bragg positions (purple ticks).

to delve into the crystalline structure in greater detail (Figure 3D, 3E and S5). Continuous lattice fringes detected from the HRTEM images in Figures 3D and 3E reveal *d*-spacing of 1.32 and 1.14 nm, which accord with that of the (110) and (002) planes, respectively, of the COF crystal structure model (Figures 3A-C, S16 and S17).

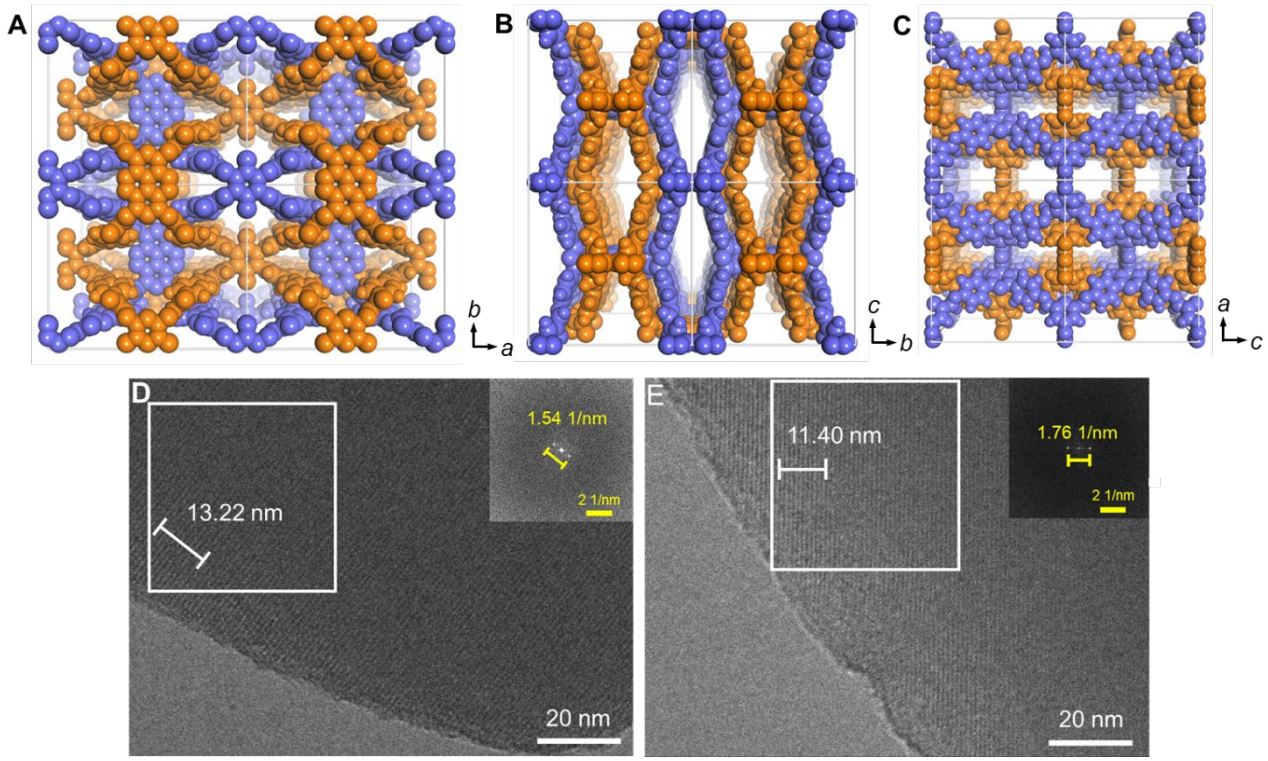


**Figure 3. Pore visualization for TUS-88.** Extended structures of TUS-88 viewed along the (A) *c*-axis, (B) *a*-axis and (C) *b*-axis. (D) HRTEM image for TUS-88. Inset: Fast Fourier Transform (FFT) pattern taken from the region marked by the white square.

### 2.3. Assessment of Porosity

The accessible pore space of TUS-88 was characterized by the nitrogen physisorption isotherms collected at 77 K across a relative pressure range extending from 0 to 1 after activating the sample overnight at 393 K. TUS-88 displayed type I isotherm hallmarked by a sharp uptake at very low relative pressures followed by a pronounced plateau, representative of the microporous nature of the COF (Figure 4A). The specific surface area deduced from the adsorption data through the use of Brunauer–Emmett–Teller (BET) model was 1688 $m^2\ g^{-1}$ (Figure S8). Besides, the pore volume of TUS-88 was obtained as 0.87 $cm^3\ g^{-1}$. The application of non-local density functional theory (NLDFT) based on the slit-pore model to the adsorption isotherms furnished a wide pore-size distribution with two clear maxima centered at 0.8 and 1.0 nm (Figure 4B), which are in good concordance with the simulated pore size. The 3D scaffold with interconnected microchannels constructed from conjugated aromatic systems like pyrene urged us to survey the adsorption affinity of TUS-88 towards $H_2$, $CO_2$ and $CH_4$, which can further extend its functionality to environmental remediation. Impressively, we observed a superlative $H_2$ uptake capacity of 188.2 $cm^3\ g^{-1}$ (8.4 mmol $g^{-1}$) at 77 K and 132.4 $cm^3\ g^{-1}$ (5.9 mmol $g^{-1}$) at 87 K, respectively, under 1 bar (Figure S9), with the maximum isosteric heat of adsorption ($Q_{st}$) quantified as 7.4 kJ $mol^{-1}$ (Figure S10). As portrayed in Figure S11, the adsorption capacity of $CO_2$ by TUS-88 reached 90.3 $cm^3\ g^{-1}$ (4.0 mmol $g^{-1}$) and 49.7 $cm^3\ g^{-1}$ (2.2 mmol $g^{-1}$) at 273 and 298 K (1 bar), respectively, and the $Q_{st}$ of $CO_2$ adsorption deduced from the adsorption isotherms was 25.2 kJ $mol^{-1}$ (Figure S12). Moreover, investigation of $CH_4$ adsorption on the COF revealed uptake capacities of 28.5 $cm^3\ g^{-1}$ (1.3 mmol $g^{-1}$) and 16.9 $cm^3\ g^{-1}$ (0.8 mmol $g^{-1}$) at 273 and 298 K (1 bar), respectively (Figure S13), based on which the $Q_{st}$ was calculated to be 17.8 kJ $mol^{-1}$ (Figure S14).

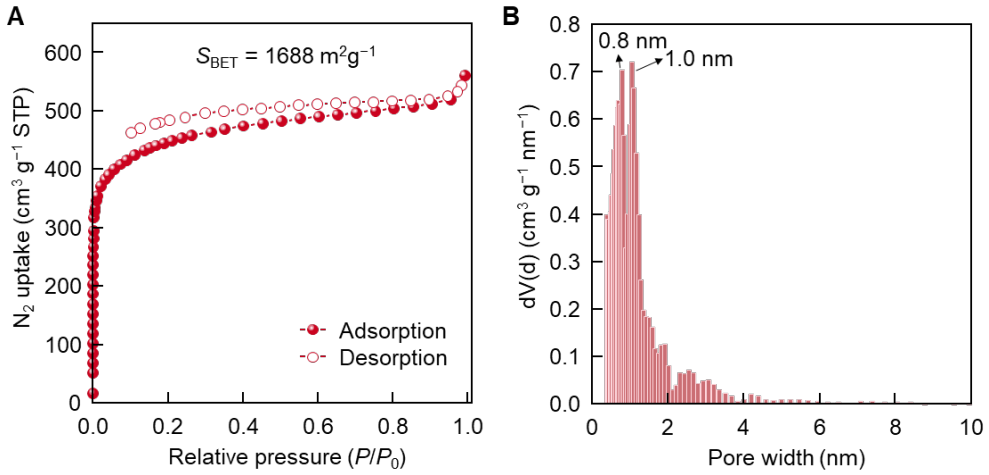


**Figure 4. Porosity characterization for TUS-88.** (A) Nitrogen sorption isotherms at 77 K and (B) pore-size distribution profile determined by NLDFT, for TUS-88.

### 2.4. Single-Component Gas Adsorption Behavior

The 3D porous architecture with rich aromatic conjugated structure of TUS-88 aroused our interest for discrimination of aromatic/non-aromatic hydrocarbon mixtures. We probed the Bz and Cy vapor uptake capacities of the COF at 298 K. As characterized by the single-component vapor sorption isotherms, a striking difference in the Bz and Cy uptakes was noticed, with the Bz uptake (1618 mg $g^{-1}$) far greater than that of Cy (842 mg $g^{-1}$) at a relative pressure of 0.98 (Figure 5A). The aromaticity of Py contributing to a conjugated system, together with the multiple aromatic phenyl rings building the COF backbone, fosters stronger π···π interactions with aromatic Bz molecules. Relatively, the binding affinity towards aliphatic Cy molecules is noticeably weaker. It is worthy of note that the Bz saturation uptake observed for TUS-88 largely outweighs all COFs like CTF-IP-10 (976 mg $g^{-1}$),[46] COF-300-rt (875

mg $g^{-1}$),[47] COF-300-st (773 mg $g^{-1}$),[47] LZU-111 (750 mg $g^{-1}$)[47] and most porous organic polymers (POPs) like PAF-1 (1306 mg $g^{-1}$),[48] MPI-1 (1198 mg $g^{-1}$),[49] POP-1 (1020 mg $g^{-1}$),[50] PCN-AD (980 mg $g^{-1}$)[51] etc. (Figure 5B, Table S2) under identical conditions. Likewise, the Cy uptake capacity of TUS-88 also surpasses those of all COFs, for example, COF-300-rt (658 mg $g^{-1}$),[47] LZU-111 (616 mg $g^{-1}$),[47] COF-300-st (500 mg $g^{-1}$),[47] and most POPs including UMC-800 (734 mg $g^{-1}$),[52] POP-1 (658 mg $g^{-1}$),[50] FJU-P7 (640 mg $g^{-1}$),[53] PCN-AD (574 mg $g^{-1}$),[51] CCTF-1 (441 mg $g^{-1}$)[54] etc. (Figure 5D, Table S2). Consequently, an ideal Bz/Cy adsorption selectivity of 1.92 was achieved for TUS-88, superior to those for earlier documented Bz-selective COFs like COF-300-st (1.55),[47] COF-300-rt (1.33),[47] LZU-111 (1.22)[47] (Table S2).

### 2.5. Breakthrough Studies with Mixed Gas

To further explore the binary gas separation performance of TUS-88, we accomplished dynamic column breakthrough tests with an equimolar Bz and Cy mixture at a flow rate of 16.2 mL $min^{-1}$ and 298 K (Figure S22). As evident from the breakthrough profiles (Figure 5C), the Cy eluted through the packed column first at 119.1 min $g^{-1}$ with a high purity of ≥99.95%, followed by Bz breaking through the column bed at 194.5 min $g^{-1}$. Consequently, there is an appreciably long interval of 75.4 min $g^{-1}$ between Cy and Bz experimental breakthrough times, which far outstrips the breakthrough times on COF-300-rt (17 min $g^{-1}$) and COF-300-st (12 min $g^{-1}$). Table S1 illustrates the adsorption capacities and diffusion coefficients of Bz and Cy, as well as the experimental Bz/Cy selectivity obtained for TUS-88. The higher adsorption capacity of Bz (73.795 $cm^3$ $g^{-1}$) relative to Cy (29.905 $cm^3$ $g^{-1}$) is suggestive of the stronger binding affinity of the framework for Bz over Cy. Unlike previous reports, the diffusion coefficients of Bz (0.0108 $cm^2$ $s^{-1}$) and Cy (0.0104 $cm^2$ $s^{-1}$) in our system were found to be very close, possibly due to the larger kinetic diameter of Cy (0.69 nm) than that of Bz (0.59 nm). Crucially, the COF showcases a record-high Bz/Cy experimental selectivity of 2.46. Moreover, the separation capability of TUS-88 was maintained with essentially identical breakthrough times for 3 consecutive cycles, signifying its admirable stability and recyclability for Bz/Cy separation (Figure S23). PXRD and FT-IR observations of recycled COF sample substantiated that the COF structure was well-preserved through the recycling tests (Figures S24 and S25).

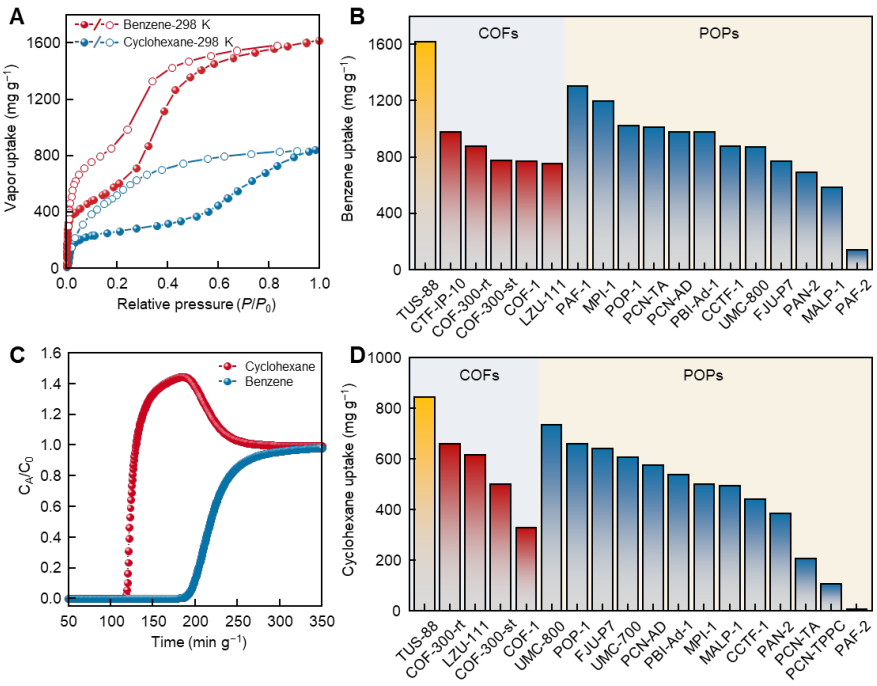

**Figure 5. Adsorptive separation of Bz and Cy by TUS-88.** (A) Bz and Cy vapor sorption (Adsorption: closed symbols, desorption: open symbols) isotherms at 298 K for TUS-88. (B) Comparative Bz uptake of TUS-88 versus other reported COFs and POPs. (C) Experimental breakthrough curves for Bz/Cy (1:1, v/v) mixture at a flow rate of 16.2 mL $min^{-1}$ in a column-bed packed with TUS-88 at 298 K and 1 bar. (D) Comparative Cy uptake of TUS-88 versus other reported COFs and POPs.

### 2.6. DFT Calculations for Insights into the Host-Guest Interaction Dynamics

To gain a deeper insight into the underlying reasons for the differential molecular recognition abilities of Bz and Cy by the microstructure of TUS-88, we employed dispersion-corrected DFT (DFT-D) calculations to determine the interaction energies between COF fragments and adsorbates. As depicted in Figure 6A-C, there are multiple C-H···π van der Waals (vdW) interactions (2.491-3.719 Å) between Cy molecules and the benzene rings. The calculated static binding energies for Cy at three binding sites I, II and III are 12.78, 13.52, and 9.20 kJ $mol^{-1}$, respectively. In contrast, Bz exhibits a more diverse array of interactions within the internal pores of the COF (Figure 6D-F). The introduction of Py-based monomers (TBAPP) into the framework imparts the framework with abundant conjugated structures, resulting in stronger π···π interactions (Site I: 3.349 Å) with planar Bz molecules. At site II, Bz molecules form short-range C-H···π vdW interactions (2.491-3.719 Å) with adjacent benzene rings. Additionally, due to the smaller steric hindrance of Bz molecules, they are more conducive to approaching the N site to form C-H···N strong hydrogen bonds (Site III: 3.034 and 3.047 Å). The calculated static binding energies for Bz molecules at the respective sites are 13.53, 14.76, and 14.48 kJ $mol^{-1}$, all of which exceed those of Cy, indicating a stronger affinity of the adsorption sites for Bz. The theoretical calculations align with the adsorption isotherms and breakthrough experimental results, further corroborating that COF with rich conjugated structures and appropriate pore sizes exhibit enhanced Bz adsorption and separation performance.

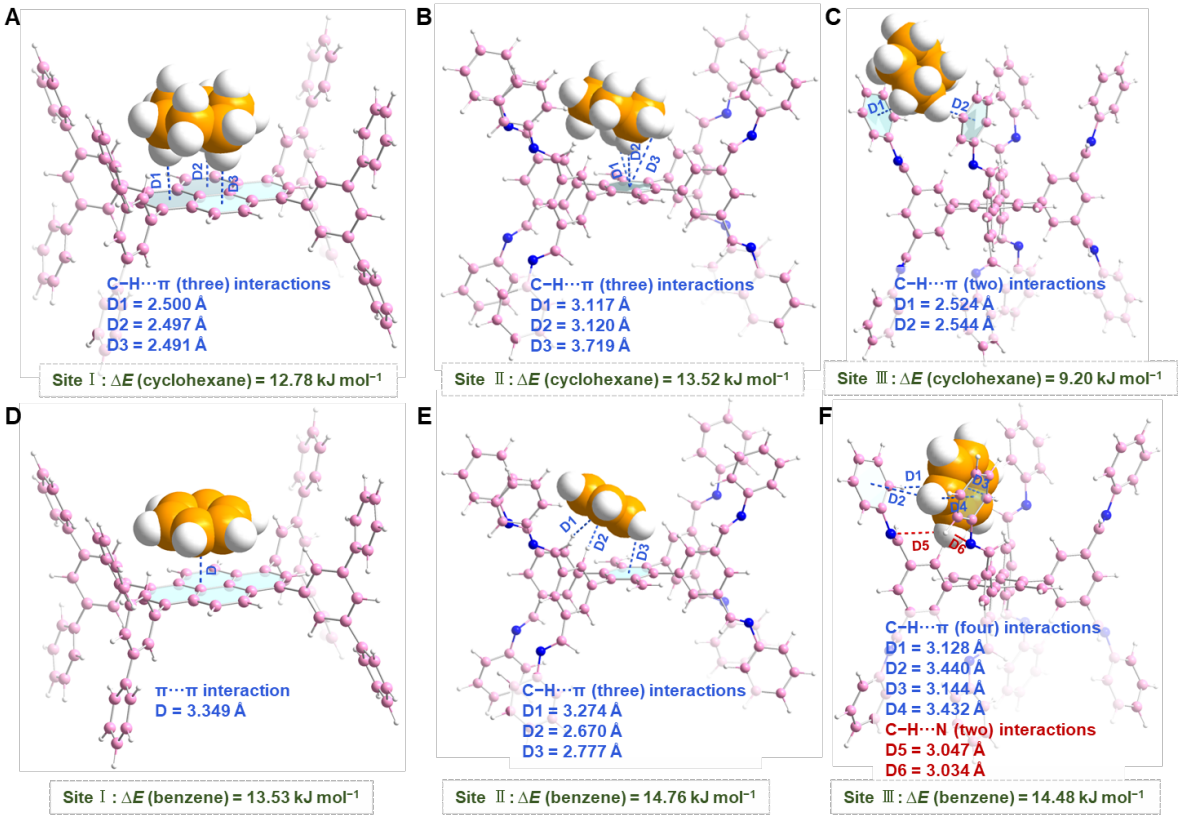


**Figure 6. Interaction energies between COF fragments and adsorbates.** (A-C) Interactions between Cy molecules and the benzene

rings of the framework, and the calculated static binding energies for Cy at three binding sites I (A), II (B) and III (C). (D-F) Interactions between Bz molecules and the benzene rings of the framework, and the calculated static binding energies for Bz at three binding sites I (D), II (E) and III (F).

## 3. Conclusion

To conclude, we report the adoption of an [8+8] imine condensation approach to developing a novel 3D COF, TUS-88, with intricate structural complexity and with the suitable pore functionality to render the efficient separation of Bz and Cy at 298 K. The **bcu-c** topology COF showcases outstanding Bz (1618 mg $g^{-1}$) and Cy (842 mg $g^{-1}$) uptakes and excellent Bz/Cy selectivity (1.92), attributable to the π···π stacking interactions between the framework and aromatic Bz resulting from the presence of π-aromatic conjugated system of pyrene and the aromatic phenyl rings in the COF network. Investigated via dynamic breakthrough measurements for equimolar Bz/Cy mixture, we noted that pure Cy elutes through the bed in a short time, whereas the COF retained the Bz with a long breakthrough time of ~75.4 min $g^{-1}$ and exhibiting an inimitable Bz/Cy experimental selectivity of 2.46. Furthermore, DFT calculations deepened our comprehension of host-guest interactions presenting additional demonstration of binding energies pertaining to π···π and C-H···π vdW interactions at different binding sites of the network for Bz and Cy molecules. Our discovery will serve as a guideline for synthetic chemists seeking to raise the connectivity of COF nets to furthering elaborate functionalities for optimization of processes springing from host-guest synergistic interactions.

## 4. Experimental Procedures

### 4.1. Synthesis of TUS-88

Typically, TBAPP (30.88 mg, 0.025 mmol) and DPTB-Me (15.86 mg, 0.025 mmol) were inserted into a Pyrex tube (volume: 10 mL, O.D. × I.D.: 10 mm × 8 mm). 1 mL of anhydrous *o*-DCB was added to the tube and the mixture was sonicated for about 10 minutes. This was followed by the addition of 0.2 mL of 9 M aqueous acetic acid and another round of 10 minutes sonication. Subsequently, 0.1 mL of aniline was added and the tube was sonicated again for another 10 minutes to ensure homogeneity. The tube was then degassed through three freeze-pump-thaw cycles, sealed under vacuum and placed in a 393 K oven for 7 days. The precipitate was isolated by centrifugation and washed with THF (5 × 10 mL) until the eluate became colorless. Further purification of the COF was executed in a Soxhlet extractor with THF for 24 hours. The powder was dried at room temperature under vacuum overnight before drying at 100 ºC under vacuum for 6 hours to give TUS-88 as a yellow solid (38.3 mg, 88% yield).

### 4.2. Breakthrough Experiments

Multi-constituent adsorption breakthrough curves were measured by BSD-MAB instrument. Before every breakthrough experiment, the column was outgassed for 8 h under vacuum at 393 K and then swept with He flow at room temperature. To continuously monitor the effluent gas from the absorption bed, a BSD-mass mass spectrometry (TCD-Thermal Conductivity Detector, detection limit 1 ppm) was used. The vapor separation properties of the COF samples were evaluated according to breakthrough experiments conducted using a Bz/Cy/He (2:2:96, v/v/v) gas mixture at a flow rate of 16.2 mL $min^{-1}$ and a temperature of 298 K. The concentration of the discharged gas mixture was continuously monitored by a multi-component mass spectrometer (BSD-MAB, INFICON) based on ion peaks detected at m/z+ values of 78 (Bz), 84 (Cy), and 4 (He).

### 4.3. DFT Calculations

The geometry of Bz, Cy and two representative fragments of the COF material were all optimized under the framework of DFT with B3LYP functional[55-57], DFT-D3 dispersion correction method and basis set of 6-31g(d)[58,59]. In order to obtain the most likely adsorption structures of Bz and Cy on these two COF fragments, two possible adsorption sites were compared. The adsorption energy of the complex was calculated from the formula:

$E(\text{adsorb}) = E(\text{A+B}) - E(\text{A}) - E(\text{B})$

where $E$(A) and $E$(B) denote the free energy of isolated molecules A and B, $E$(A+B) denotes the total energy of the complex structure.

The Independent gradient model (IGM)[60] which is a visualized weak interaction analysis method was performed to investigate the intermolecular interaction. The visualization of the frontier molecular orbitals and mapping of IGM were all rendered using Visual Molecular Dynamics (VMD) program.[61]


### ACKNOWLEDGMENTS

This study received funding from the National Key R&D Program of China (2021YFA1200400), the NSFC (91956108, 22201256), and the Natural Science Foundation of Zhejiang Province (LZ22B010001). Financial support from the JSPS KAKENHI (grant no. 20H02698 and 20H02552), Scientific Research on Innovative Areas “Aquatic Functional Materials” (grant no. 22H04562), the Yazaki Memorial Foundation for Science and Technology, and the Ogasawara Foundation for the Promotion of Science and Engineering is also gratefully acknowledged.


### References


1. Sholl, D.S., and Lively, R.P. (2016). Seven chemical separations to change the world. Nature 532, 435–437. 10.1038/532435a.

2. https://www.chemanalyst.com/industry-report/benzene-market-56.

3. Neves, E.S., Fernandes, C., and Horn, Jr. A. (2023). Study of Cyclohexane and Methylcyclohexane Functionalization Promoted by Manganese(III) Compounds. Inorganics 11, 105. 10.3390/inorganics11030105.

4. Ma, S., Li, J., Li, L., Shang, X., Liu, Shikai., Xue, C., and Sun, L. (2018). Liquid–Liquid Extraction of Benzene and Cyclohexane Using Sulfolane-Based Low Transition Temperature Mixtures as Solvents: Experiments and Simulation. Energy Fuels 32, 8006–8015. 10.1021/acs.energyfuels.8b01524.

5. https://www.globallcadataaccess.org/cyclohexane-production-upr-ecoinvent-36-allocation-apos

6. Dong, H., Yang, X., Yue, G., Cao, W., and Zhang, J. (2011). Liquid−Liquid Equilibria for Benzene + Cyclohexane + N,N-Dimethylformamide + Ammonium Thiocyanate. J. Chem. Eng. Data 56, 2664–2668. 10.1021/je1012026.

7. Zhang, J.-P., and Chen, X.-M. (2008). Exceptional Framework Flexibility and Sorption Behavior of a Multifunctional Porous Cuprous Triazolate Framework. J. Am. Chem. Soc. 130, 6010–6017. 10.1021/ja800550a.

8. Villaluenga, J.P.G., and Tabe-Mohammadi, A. (2000). A review on the separation of benzene/cyclohexane mixtures by pervaporation processes. J. Membr. Sci. 169, 159–174. 10.1016/s0376-7388(99)00337-3.

9. Lue, S.J., Wang, F.J., and Hsiaw, S.-Y. (2004). Pervaporation of benzene/cyclohexane mixtures using ion-exchange membrane containing copper ions. J. Membr. Sci. 240, 149–158. 10.1016/j.memsci.2004.05.003.

10. Wang, X., Xu, H., Zou, Y., Hu, W., and Wang, L. (2022). Mechanistic insight into separation of benzene and cyclohexane by extractive distillation using deep eutectic solvent as entrainer. J. Mol. Liq. 368, 120780. 10.1016/j.molliq.2022.120780.

11. Salleh, Z, Wazeer, I., Mulyono, S., El-blidi, Lahssen., Hashim, M.A. and Hadj-Kali, M.K. (2017). Efficient removal of benzene from cyclohexane-benzene mixtures using deep eutectic solvents – COSMO-RS screening and experimental validation. J. Chem. Thermodyn. 104, 33–44. 10.1016/j.molliq.2022.120780.

12. Dong, Y., Guo, H., Su, Z., Wei, W., and Wu, X. (2015). Pervaporation separation of benzene/cyclohexane through AAOM-ionic liquids/polyurethane membranes. Chem. Eng. Process. 89, 62–69. 10.1016/j.cep.2015.01.006.

13. Acharya, H.R., Stern, S.A., Liu, Z.Z., and Cabasso, I. (1988). Separation of liquid benzene/cyclohexane mixtures by perstraction and pervaporation. J. Membr. Sci. 37, 205–232. 10.1016/S0376-7388(00)82430-8.

14. Yaghi, O.M., Kalmutzki, M.J., Diercks, C.S. (2019). Introduction to Reticular Chemistry: Metal-Organic Frameworks and Covalent Organic Frameworks, Wiley-VCH: Weinheim, Germany, 2019, ch. 7-11, pp. 177-283.

15. Waller, P.J., Gándara, F., and Yaghi, O.M. (2015). Chemistry of Covalent Organic Frameworks. Acc. Chem. Res. 48, 3053–3063. 10.1021/acs.accounts.5b00369.

16. Ding, S.-Y., and Wang, W., (2013). Covalent organic frameworks (COFs): from design to applications. Chem. Soc. Rev. 42, 548–568. 10.1039/C2CS35072F.

17. Tan, K.T., Ghosh, S., Wang, Z., Wen, F., Rodríguez-San-Miguel, D., Feng, J., Huang, N., Wang, W., Zamora, F., Feng, X., et al. (2023). Covalent organic frameworks. Nat. Rev. Methods Primers 3, 1. 10.1038/s43586-022-00181-z.

18. Haase, F., and Lotsch, B.V. (2020). Solving the COF trilemma: towards crystalline, stable and functional covalent organic frameworks. Chem. Soc. Rev. 49, 8469–8500. 10.1039/D0CS01027H.

19. Keller, N., and Bein, T. (2021). Optoelectronic processes in covalent organic frameworks. Chem. Soc. Rev. 50, 1813–1845. 10.1039/D3CS00703K.

20. Kandambeth, S., Dey, K., and Banerjee, R. (2019). Covalent Organic Frameworks: Chemistry beyond the Structure. J. Am. Chem. Soc. 141, 1807–1822. 10.1021/jacs.8b10334.

21. Zhao, X., Pachfule, P., and Thomas, A. (2021). Covalent organic frameworks (COFs) for electrochemical applications. Chem. Soc. Rev. 50, 6871–6913. 10.1039/d0cs01569e.

22. Song, Y., Sun, Q., Aguila, B., and Ma, S. (2019). Opportunities of Covalent Organic Frameworks for Advanced Applications. Adv. Sci. 6, 1801410. 10.1002/advs.201801410.

23. Li, Y., Chen, W., Xing, G., Jiang, D., and Chen, L. (2020). New synthetic strategies toward covalent organic frameworks. Chem. Soc. Rev. 49, 2852–2868. 10.1039/d0cs00199f.

24. Han, X., Yuan, C., Hou, B., Liu, L., Li, H., Liu, Y., and Cui, Y. (2020). Chiral covalent organic frameworks: design, synthesis and property. Chem. Soc. Rev. 49, 6248–6272. 10.1039/d0cs00009d.

25. Li, X., Yadav, P., and Loh, K.P. (2020). Function-oriented synthesis of two-dimensional (2D) covalent organic frameworks – from 3D solids to 2D sheets. Chem. Soc. Rev. 49, 4835–4866. 10.1039/d0cs00236d.

26. Guan, X., Chen, F., Fang, Q., and Qiu, S. (2020). Design and applications of three dimensional covalent organic frameworks. Chem. Soc. Rev. 49, 1357–1384. 10.1039/c9cs00911f.

27. Qian, C., Feng, L., Teo, W.L., Liu, J., Zhou, W., Wang, D., and Zhao, Y. (2022). Imine and imine-derived linkages in two-dimensional covalent organic frameworks. Nat. Rev. Chem. 6, 881–898. 10.1038/s41570-022-00437-y.

28. Huang, J., Han, X., Yang, S., Cao, Y., Yuan, C., Liu, Y., Wang, J., and Cui, Y. (2019). Microporous 3D Covalent Organic Frameworks for Liquid Chromatographic Separation of Xylene Isomers and Ethylbenzene. J. Am. Chem. Soc. 141, 8996–9003. 10.1021/jacs.9b03075.

29. Huang, J., Shi, Y., Xu, J., Zheng, J., Zhu, F., Liu, X., and Ouyang, G. (2022). Hollow Covalent Organic Framework with “Shell-Confined” Environment for the Effective Removal of Anionic Per- and Polyfluoroalkyl Substances. Adv. Funct. Mater. 32, 2203171. 10.1002/adfm.202203171.

30. He, Y., Lin, X., Zhou, Y., Chen, J.H., Guo, Z., and Zhan, H. (2021). Synthesizing Highly Crystalline Self-Standing Covalent Organic Framework Films through a Homogeneous–Floating–Concentrating Strategy for Molecular Separation. Chem. Mater. 33, 9413–9424. 10.1021/acs.chemmater.1c03414.

31. Fan, H., Peng, M., Strauss, I., Mundstock, A., Meng, H., and Caro, J. (2020). High-Flux Vertically Aligned 2D Covalent Organic Framework Membrane with Enhanced Hydrogen Separation. J. Am. Chem. Soc. 142, 6872–6877. 10.1021/jacs.0c00927.

32. Pütz, A.M., Terban, M.W., Bette, S., Haase, F., Dinnebier, R.E., and Lotsch, B.V. (2020). Total scattering reveals the hidden stacking disorder in a 2D covalent organic framework. Chem. Sci. 11, 12647–12654. 10.1039/d0sc03048a.

33. Guan, X., Fang, Q., Yan, Y., and Qiu, S. (2022). Functional Regulation and Stability Engineering of Three-Dimensional Covalent Organic Frameworks. J. Am. Chem. Soc. 130, 1833–1836. 10.1021/acs.accounts.2c00200.

34. Nouar, F., Eubank, J.F., Bousquet, Till., Wojtas, L., Zaworotko, M.J., and Eddaoudi, M. (2008). Supermolecular Building Blocks (SBBs) for the Design and Synthesis of Highly Porous Metal-Organic Framework. Acc. Chem. Res. 55, 1912–1927. 10.1021/ja710123s.

35. Shan, Z., Wu, M., Zhu, D., Wu, X., Zhang, K., Verduzco, R., and Zhang, G. (2022). 3D Covalent Organic Frameworks with Interpenetrated pcb Topology Based on 8 Connected Cubic Nodes. J. Am. Chem. Soc. 144, 5728–5733. 10.1021/jacs.2c01037.

36. Jin, F., Lin, E., Wang, T., Geng, S., Wang, T., Liu, W., Xiong, F., Wang, Z., Chen, Y., Cheng, P., et al. (2022). Bottom-Up Synthesis of 8 Connected Three-Dimensional Covalent Organic Frameworks for Highly Efficient Ethylene/Ethane Separation. J. Am. Chem. Soc. 144, 5643–5652. 10.1021/jacs.2c01058.

37. Das, S., Mabuchi, H., Irie, T., Sasaki, K., Nozaki, M., Tomioka, R., Wen, D., Zhao, Y., Ben, T., Negishi, Y. (2023). Three-Dimensional Covalent Organic Framework with “the” Topology. ChemRxiv. 10.26434/chemrxiv-2023-pzbz4.

38. Das, S., Sekine, T., Mabuchi, H., Irie, T., Sakai, J., Zhao, Y., Fang, Q., and Negishi, Y. (2022). Three-Dimensional Covalent Organic Framework with scu-c Topology for Drug Delivery. ACS Appl. Mater. Interfaces. 14, 48045–48051. 10.1021/acsami.2c15152.

39. Jin, F., Lin, E., Wang, T., Yan, D., Yang, Y., Chen, Y., Cheng, P., and Zhang, Z. (2022). Rationally fabricating 3D porphyrinic covalent organic frameworks with scu topology as highly efficient photocatalysts. Chem 8, 3064–3080. 10.1016/j.chempr.2022.07.016.

40. Liu, W., Wang, K., Zhan, X., Liu, Z., Yang, X., Jin, Y., Yu, B., Gong, L., Wang, H., Qi, D., et al. (2023). Highly Connected Three-Dimensional Covalent Organic Framework with Flu Topology for High-Performance Li S Batteries. J. Am. Chem. Soc. 145, 8141–8149. 10.1021/jacs.3c01102.

41. Fu, Z., and Xu, G. (2016). Crystalline, Highly Oriented MOF Thin Film: the Fabrication and Application. Chem. Rec. 17, 1–18. 10.1002/tcr.201600109.

42. Das, P., and Mandal, S.G. (2018). A dual-functionalized, luminescent and highly crystalline covalent organic framework: molecular decoding strategies for VOCs and ultrafast TNP sensing. J. Mater. Chem. A 6, 16246–16256. 10.1039/c8ta05070h.

43. Das, P., and Mandal, S.G. (2019). In-Depth Experimental and Computational Investigations for Remarkable Gas/Vapor Sorption, Selectivity, and Affinity by a Porous Nitrogen-Rich Covalent Organic Framework. Chem. Mater. 31, 1584–1496. 10.1021/acs.chemmater.8b04683.

44. http://rcsr.net/nets

45. Materials Studio, ver. 7.0; Accelrys Inc.: San Diego, CA.

46. Karmakar, A., Kumar, A., Chaudhari, A.K., Samanta, P., Desai, A.V., Krishna, R., and Ghosh, S.K. (2016). Bimodal Functionality in a Porous Covalent Triazine Framework by Rational Integration of an Electron-Rich and -Deficient Pore Surface. Chem. - Eur. J. 22, 4931−4937. 10.1002/chem.201600109.

47. Moroni, M., Roldan-Molina, E., Vismara, R., Galli, S., and Navarro, J.A.R. (2022). Impact of Pore Flexibility in Imine-Linked Covalent Organic Frameworks

on Benzene and Cyclohexane Adsorption. ACS Appl. Mater. Interfaces 14, 40890−40901. 10.1021/acsami.2c09911.

48. Ben, T., Ren, H., Ma, S., Cao, D., Lan, J., Jing, X., Wang, W., Xu, J., Deng, F., Simmons, J.M., et al. (2009). Targeted synthesis of a porous aromatic framework with high stability and exceptionally high surface area. Angew. Chem., Int. Ed. 48, 9457−9460. 10.1002/anie.200904637.

49. Li, G., and Wang, Z. (2013). Microporous Polyimides with Uniform Pores for Adsorption and Separation of CO2 Gas and Organic Vapors. Macromolecules 46, 3058−3066. 10.1021/ma400496q.

50. Tan, H., Chen, Q., Chen, T., and Liu, H. (2018). Selective Adsorption and Separation of Xylene Isomers and Benzene/Cyclohexane with Microporous Organic Polymers POP-1. ACS Appl. Mater. Interfaces 10, 32717−32725. 10.1021/acsami.8b11657.

51. Shen, C., Yu, H., and Wang, Z. (2014). Synthesis of 1,3,5,7-tetrakis(4-cyanatophenyl)adamantane and its microporous polycyanurate network for adsorption of organic vapors, hydrogen and carbon dioxide. Chem. Commun. 50, 11238−11241. 10.1039/C4CC05021E.

52. Yan, J., Zhang, B., and Wang, Z. (2017). Ultramicroporous Carbons Derived from Semi-Cycloaliphatic Polyimide with Outstanding Adsorption Properties for H2, CO2, and Organic Vapors. J. Phys. Chem. C 121, 22753−22761. 10.1021/acs.jpcc.7b06133.

53. Chen, L., Zhang, H., Ye, Y., Yuan, Z., Wang, J., Yang, Y., Lin, S., Xiang, F., Xiang, S., and Zhang, Z. (2021). Microporous polycarbazole frameworks with large conjugated p systems for cyclohexane separation from cyclohexane-containing mixtures. New J. Chem. 45, 22437−22443. 10.1039/D1NJ04968B.

54. Yan, J., Sun, H., Wang, Q., Lu, L., Zhang, B., Wang, Z., Guo, S., and Han, F. (2022). Covalent triazine frameworks for the dynamic adsorption/separation of benzene/cyclohexane mixtures. New J. Chem. 46, 7580−7587. 10.1039/d2nj00727d.

55. Becke, A.D. (1988). Density-functional exchange-energy approximation with correct asymptotic behavior. Phys. Rev. A 38, 3098. 10.1103/PhysRevA.38.3098.

56. Lee, C., Yang, W., and Parr, R.G. (1988). Development of the Colle-Salvetti correlation-energy formula into a functional of the electron density. Phys. Rev. B 37, 785. 10.1103/PhysRevB.37.785.

57. Becke, A.D. (1992). Density-functional thermochemistry. I. The effect of the exchange-only gradient correction. J. Chem. Phys. 96, 2155–2160. 10.1063/1.462066.

58. Petersson, G.A., Bennett, A., Tensfeldt, T.G., Al-Laham, M.A., Shirley, W.A., and Mantzaris, J. (1988). A complete basis set model chemistry. I. The total energies of closed-shell atoms and hydrides of the first-row elements. J. Chem. Phys. 89, 2193–2218. 10.1063/1.455064.

59. Petersson, G.A., and Al-Laham, M.A. (1991). A complete basis set model chemistry. II. Open-shell systems and the total energies of the first-row atoms. J. Chem. Phys. 94, 6081–6090. 10.1063/1.460447.

60. Lefebvre, F., Khartabil, H., Boisson, J.-C., Contreras-García, J., Piquemal, J.-P., and Hénon, E. (2018). The Independent Gradient Model: A New Approach for Probing Strong and Weak Interactions in Molecules from Wave Function Calculations. ChemPhysChem 19, 724–735. 10.1002/cphc.201701325.

61. Humphrey, W., Dalke, Andrew., Schulten, K. (1996). J. Mol. Graphics. 14, 33-38. 10.1016/0263-7855(96)00018-5.